Light Redistribution in Variable 3D-Printed Thermoplastic Geometries

Automated optics experiments and machine learning

Yuan Zhang[1], *Hao Hua*[2],
[1,2]*Southeast University*
Zhang_yuan@seu.edu.cn, whitegreen@seu.edu.cn

The differentiated processes of 3D-printed translucent components create an unprecedented design space for both indoor optical and thermal control and novel façade tectonics. However, the impact of 3D-printed geometries on optical behaviors remains underexplored. This study proposes a systematic approach combing automated robotic experiments and machine learning, investigating how geometric parameters influence light distribution from massive data points. Initial experiments involving a single 3D-printed specimen demonstrate the feasibility of the methodology and demonstrate the potential of using machine learning in modeling light redistribution. These findings offer valuable insights into the complex optical behaviors of 3D-printed thermoplastic façades, laying a foundation for future studies to refine predictive accuracy and expand the dataset. This work highlights novel opportunities for advancing parametric design and fabrication techniques for optical façades.

Keywords: *3D-Printed Façade*, *Light Redistribution*, *Robot Arm*, *Optics*, *Machine Learning*

INTRODUCTION

Customized façade systems featuring sophisticated geometries and differentiated transparency are becoming increasingly prevalent in contemporary architectural practice. These façades provide rich visual effects and adaptive responses to climatic conditions though their construction remains challenging and costly. Recent advancements in material science and digital fabrication have facilitated the development of 3D-printed façades. The primary advantage of additive manufacturing (AM), or 3D printing, lies in its ability to fabricate intricate geometries using mono-material without molds (Naboni and Jakica, 2022). AM processes enhance design flexibility and customization while minimizing material waste (Mungenast, 2019). By integrating parametric design methodologies with AM, our approach encodes the material properties, manufacturing constraints, and optical performance coherently into the design process of 3D-printed façade, enabling continuous differentiation of its optical behaviors.

Related works

3D-printed thermoplastic façade (3DPTF) has exhibited capabilities in controlling light and thermal conditions, considering both aesthetic and functional objectives (Leschok *et al.*, 2023). Light control can take effect at multiple levels: the overall façade geometry can be tailored to the role of the building envelope (Seshadri *et al.*, 2021); the AM-produced layers influence light distribution and

transmission (Cheibas *et al.*, 2023); and intrinsic material properties, along with fabrication factors, impact the physical quality of the 3D-printed specimens—such as transparency and stiffness (Piccioni *et al.*, 2023).

To fully understand the potential of 3DPTF in customizing light environments, two research questions arise: how to systematically record and describe the way light is refracted and then redistributed when passing through the 3DPTF, and how the design & manufacturing factors influence the optical behavior.

Existing studies have employed both simulation-based and experiment-based approaches. One widely used method is the bidirectional scattering distribution function (BSDF), which characterizes the angular distribution of transmitted or reflected light for any given incident angle (Wang *et al.*, 2022). BSDF data can be obtained either through physical measurements using goniophotometers or via simulation tools such as Radiance (Kurt, 2018). Another empirical method is the use of high dynamic range (HDR) imaging, which captures luminance information from real-world lighting scenarios to visualize light distribution patterns and visual comfort (Weber, Reinhart and Oxman, 2020).

Performance characteristics of 3DPTF emerge from a coupled multi-physical phenomenon involving optical, thermal and airflow, influenced by material properties, fabrication parameters, and geometry across multiple scales (Piccioni *et al.*, 2023). Experimental or data-driven modeling approaches can encode these factors into predictive models, toward a better formulation of 3DPTF behaviors. Although previous studies have shown the potential of modeling light redistribution through 3DPTFs, a comprehensive and generalizable optical model has yet to be established.

In response to this gap, this research proposes an integrated pipeline combining parametric design, optical experimentation, and machine learning. The aim is to formulate a predictive function that relates the variable geometry and fabrication parameters of 3DPTFs to their resulting light redistribution patterns.

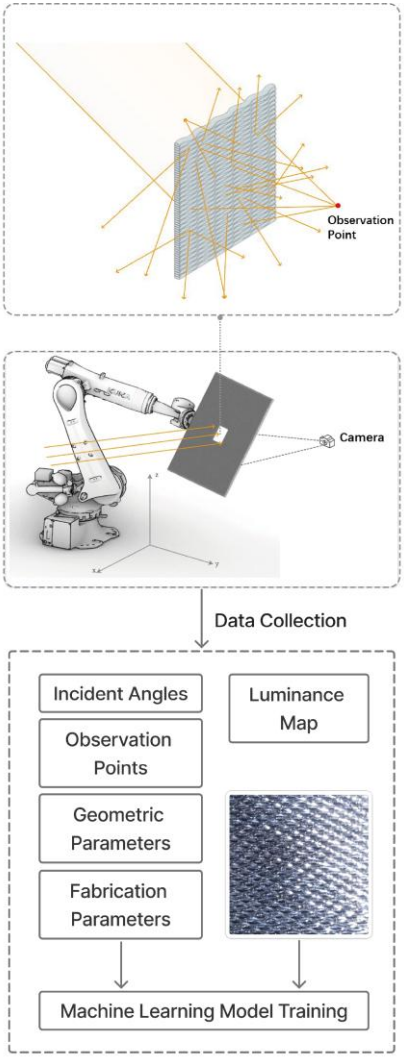

Figure 1
Research purpose and methodology diagram

METHODOLOGY

The optical development, as shown in figure 1 of 3DPTF includes (1.) parametrization and manufacturing of 3DPTF components; (2.) automated batch measurement of the luminance distribution of the 3DPTF specimens under directional light. (3.) creating a map from design variables to the luminance distribution of the 3DPTF. This map can then facilitate the façade design for inhabitant comfort and energy concerns.

Parametric design and fabrication of 3DPTF components

The surface of 3DPTF is modelled as single layer of 3D-printed transparent filament whose geometry is differentiated in a parametric manner, so that a map from the design parameters to the 3DPTF behaviors can be studied.

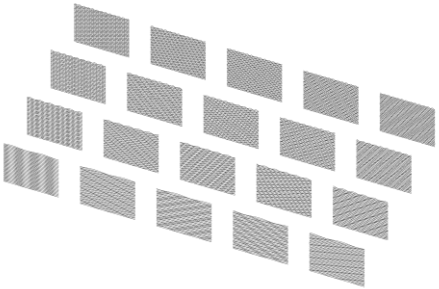

Figure 2
Geometry variations of tool path

Parametric model. A sine function forms the basis for the parametric model:

$$y = \begin{cases} 0, & if\ i\ is\ even \\ a\ sin\left(\frac{2\pi n}{100}x + \frac{i\pi}{2}p\right), & otherwise \end{cases} \qquad (1)$$
$$z = i\,h$$

where parameter *a* denotes the amplitude of the sine wave, ranging from 2mm to 4mm; parameter $n \in \{0, 1, 3, 5, 7\}$ determines the frequency; integer variable $0 \leq p \leq 4$ controls the phase shift between layers; *i* denotes the layer index. Model (1) alternates straight and curves in odd and even layers to reconcile structural support with surface freedom.

The parametric model produced 41 geometries for 3D-printing, see figure 2. Each printed specimen measures 180 × 180 mm with an interlayer spacing of 3 mm.

Robotic 3D-printing. The robotic 3D-printing process, see figure 3, was refined to ensure transparency, smoothness, and stability of the 3DPTF specimens. The KUKA robotic arm, equipped with an extrusion nozzle, printed all specimens with pre-dried PCTG (skygreen JN200) pellets in 210 ℃. The printing path was controlled using our customized program and followed a circular organization consisting of 11 specimens to extend the path length and cooling time to prevent collapse.

Figure 3
Robotic 3D-printing with PCTG pellets

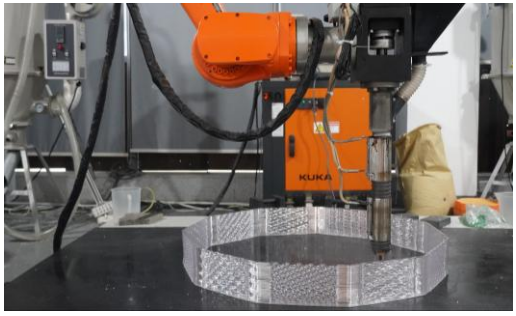

Automated optical experiments

The optical experiments should simulate real-world scenarios where façade elements fixed in buildings while both the light sources and observers' positions could change. However, the relative positions between the relevant elements (façade, light source, and observer) instead of the realistic positions of the elements are implemented in the experiments. The setup was designed to systematically collect massive data from façade geometry with full automation. The key elements include the incident directional light, observer position (represented by the camera), and luminance distribution by the 3DPTF specimens.

Experimental setup. A 30W LED spotlight (6500K, 15° beam angle) simulates the sunlight outdoor, while a Canon EOS 6D camera, simulating an indoor observer, captures the observation of the lighted specimen. Both the light source and the camera is fixed, while the 3D-printed specimen in between is movable by a robot arm, as shown in figure 4. A 1.2m × 1.2m aluminum frame is mounted onto the KUKA robot to hold specimens, with a chessboard PVC plate (2mm thick) for camera calibration and light blocking. To ensure accurate positioning, the center point of rectangular specimen is designated as the TCP (Tool Center Point) of the robot.

The camera and light source were fixed on tripods, positioned on either side of the specimen. Their relative locations and orientations were obtained through camera calibration. The camera settings were adjusted based on existing research and experimental conditions to ensure high image quality, sharp details, and a neutral color balance (Pierson *et al*., 2021). A relay module serves as an intermediary switch that controls the camera's shutter release. The robotic arm sends a digital output signal to the relay module, which then completes the circuit to trigger the camera.

In the exposure bracketing mode, each scene is captured at five different exposure levels, generating low dynamic range (LDR) images, which are later used for creating high dynamic range (HDR) image to better represent real-world luminance distribution.

To enable systematic data collection, two key steps were implemented:

- Path Planning: Moving and rotating the specimen via the robotic arm to alter its relative position to the camera/light source.
- Camera Calibration: Determining the position and orientation of the camera in the reference coordinate system.

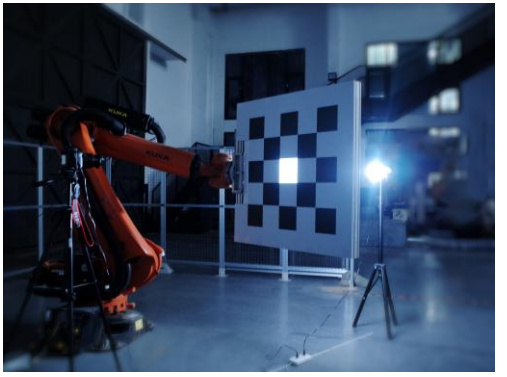

Figure 4
Setup of the automated optical experiment

Toolpath planning. To maximize deviations in relative positioning with minimal specimen movement, both rotation and translation were employed. Experimental trials indicated that rotations within ± 20° did not introduce light leakage, while translations up to ±250 mm ensured the specimen remained within the camera's field of view. Based on these constraints, the final motion path was designed to uniformly cover the valid design space of relative positions. A 5 × 5 grid was defined, each spaced 50mm apart. At each grid point, the specimen was rotated along the X, Y, and Z axes respectively within a -20° to 20° range at 10° increments, resulting in $5^3 = 125$ instances.

The robotic system totally produced 3125 states in which the specimen's relative position to the camera and to the light source vary (refer to figure 5). The specimen's trajectory, the camera's position

relative to the specimen, and the light source's position relative to the specimen are illustrated in the figure 5.

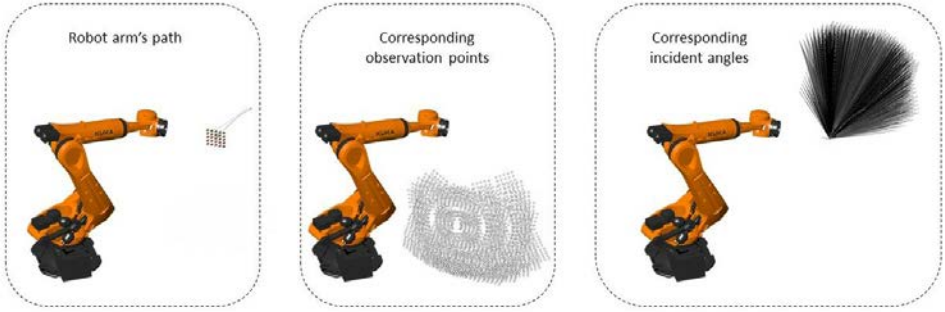

Figure 5
Relative positions between the specimen movements, observation points and incident lights

Camera calibration. In the pinhole camera model, any point $\mathrm{Pw(X,Y,Z)}$ in the reference coordinate system is uniquely projected onto the image plane as a pixel $\mathrm{p(u,v)}$ (Damirchi, Khorrambakht and Taghirad, 2019), see figure 6. The transformation from 3D coordinates to 2D pixel coordinates involves sequential conversions through the world, camera, image, and pixel coordinate system (Huang *et al.*, 2023).

$$Z_c \begin{bmatrix} u \\ v \\ 1 \end{bmatrix} = T \begin{bmatrix} X_w \\ Y_w \\ Z_w \\ 1 \end{bmatrix} = KM \begin{bmatrix} X_w \\ Y_w \\ Z_w \\ 1 \end{bmatrix}$$

$$= \begin{bmatrix} \frac{f}{dx} & 0 & u_0 & 0 \\ 0 & \frac{f}{dy} & v_0 & 0 \\ 0 & 0 & 1 & 0 \end{bmatrix} \begin{bmatrix} R & t \\ 0^T & 1 \end{bmatrix} \begin{bmatrix} X_w \\ Y_w \\ Z_w \\ 1 \end{bmatrix} \quad (2)$$

The transformation can be expressed in Equation (2), where Z_c is an unknown scale factor along the z-axis of the camera; T denotes the projection matrix; K denotes the camera intrinsic matrix; M denotes the camera extrinsic matrix; dx and dy (mm/pixel) are the actual physical sizes corresponding to a single pixel; (u_0, v_0) are the pixel coordinates of the image center.

The intrinsic parameters are determined following the least-squares approach (Zhang, 2000) which captures images of a 2D chessboard from various angles. The camera's extrinsic parameters — its position and orientation in the reference coordinate system — were obtained by solving the Perspective-n-Point (PnP) problem using the physical coordinates of chessboard corners and their corresponding pixel positions in the captured images. The transformation from robot's pose to physical coordinates is given by:

$$^1P = T_1{}^{-1} T_2 P \quad (3)$$

Where T_1 denotes the transformation matrix from the world coordinate system to the reference coordinate system; T_2 denotes the transformation matrix from the world coordinate system to the TCP pose at any given position; ^1P represents the 3D coordinates of the chessboard corner points in reference coordinate system, which is the desired value. To improve robustness against single-image discrepancies, bundle adjustment was applied to minimize the overall reprojection error.

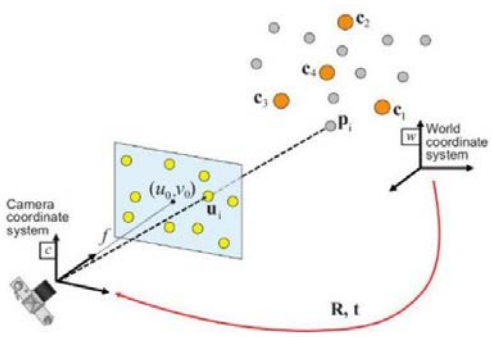

Figure 6
Principle and implementation of camera calibration

Data processing and machine learning

After collecting the batch photographs of the luminance surfaces under light, further processing was performed to generate paired dataset used for machine learning. Each sample consists of observation point transformations and the incident angle relative to the specimen and corresponding luminance maps, ensuring structured training data for training predictive models.

Camera and light source position transformation. Given the camera's coordinate ${}^{r}_{c}P$ represented by extrinsic parameters and the robot's poses (X, Y, Z, A, B, C), the spatial coordinates and viewing directions of the camera ${}^{s}_{c}P$ relative to the specimen can be derived using the following equation.

$$ {}^{s}_{c}P = \begin{bmatrix} R & t \\ 0 & 1 \end{bmatrix}^{-1} {}^{r}_{c}P \qquad (4) $$

The incident and azimuth angle (θ, φ), can be derived from the coordinate of the light source P_i and TCP P_s , and the normal N of the specimen (aligned with the z-axis of the TCP coordinate system):

$$ L = P_s - P_i \qquad (5) $$

$$ \theta = \cos^{-1}\left(\frac{L \cdot N}{\| L \| \ \| N \|} \right) \qquad (7) $$

Luminance map. HDR images are used as luminance maps to capture the luminance from a specific point of the lighted specimen, recording the luminous intensity (cd/㎡) emitted from that point towards the observation point (Jacobs, 2007). Using the Radiance's hdrgen function, five images taken at different exposure levels are merged into a single HDR image. However, due to inaccuracies in camera's shooting process, luminance calibration has to be applied using a luminance meter in order to obtain the absolute luminance value of the scene (Jacobs, 2007). Since only a portion of each high-resolution full-frame image is needed for training, the relevant specimen area is cropped from the HDR image and resized to 800×800 pixels coupled with a transformation matrix, as shown in figure 7.

Machine learning. Prior to data training, the HDR luminance maps undergo preprocessing: RGB pixel values are first converted into single channel of luminance value using $0.2126\mathrm{R} + 0.7152\mathrm{G} + 0.0722\mathrm{B}$followed by min-max normalization to the range [0,1] and compression to a lower resolution of 128×128 pixels.

Figure 7
Luminance map synthesized by Radiance

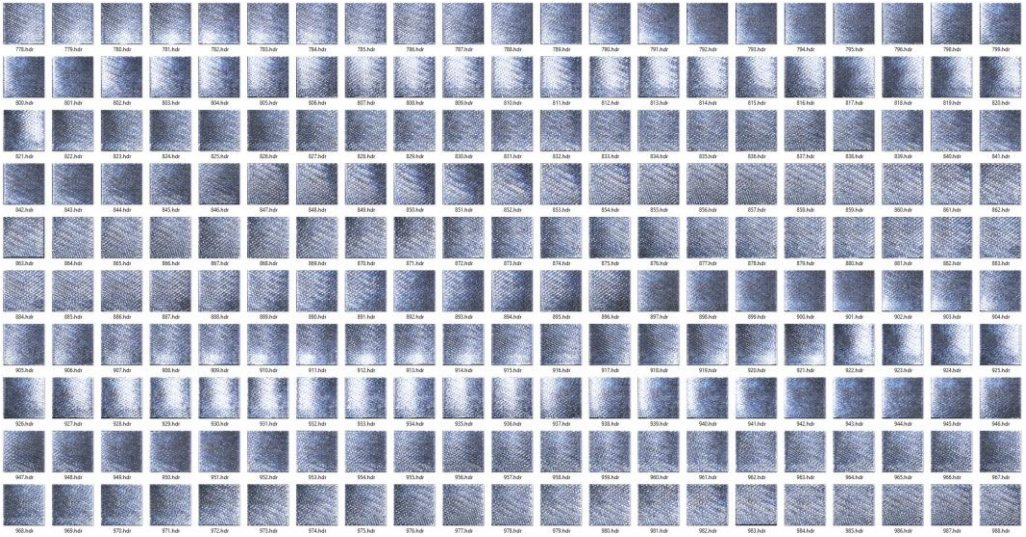

Figure 8
The two-stage machine learning model

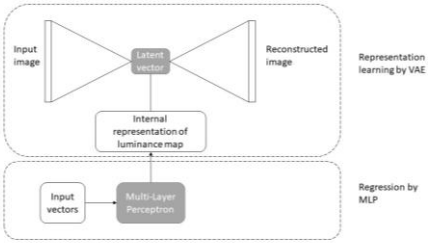

We employ a VAE+MLP architecture (refer to figure 8) for supervised learning, as is suited for small datasets of this scale (3,108 samples in our case). The variational autoencoder (VAE) serves as a feature extractor, utilizing a convolutional encoder-decoder structure to compress luminance photos into a lower-dimensional latent space representation, while enabling reconstruction of luminance images from the latent vectors. The multilayer perceptron (MLP) learns to map the input vector (including geometric parameters, fabrication parameters, observation points, and incident angles) to the latent representation which can be subsequently decoded into luminance images by the VAE decoder.

During model training, the dataset is split into training (75%), validation (15%), and test (15%) sets. Once the VAE is trained, it is used to extract latent vectors from all data, which then serve as outputs for MLP regression. The structural similarity index measure (SSIM) is used as the loss function in the VAE training, as it evaluates luminance, contrast and structure of the image, while mean squared error (MSE) is employed for MLP training. Finally, the trained model is validated through visual comparisons using the test set.

EXPERIMENTS AND RESULTS

Due to the complexity of the experiment and computational process, this study initially focuses on modeling the light distribution of a single specimen to validate the experimental methodology, data processing pipeline, and machine learning strategy. Our future work will extend the approach to larger datasets for establishing a comprehensive mapping from geometric parameters to light redistribution.

Each experimental cycle for a single specimen took approximately 3 hours without any manual intervention, demonstrating the efficiency of the

automated system. The experiment captured 16,500 images, from which 3,108 luminance maps were successfully generated.

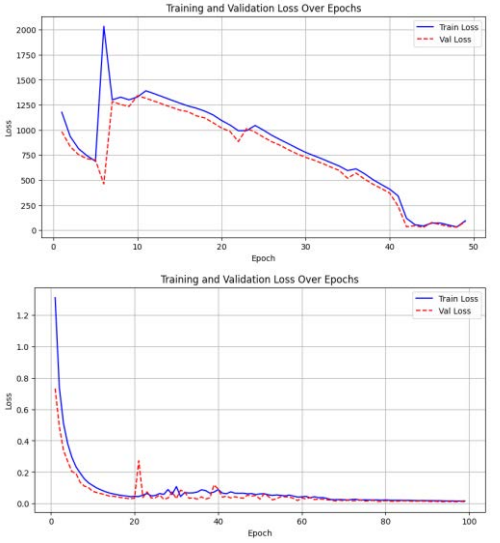

Figure 9
The loss curve of VAE training and MLP training

The training is implemented using PyTorch, with multiple trials adjusting the learning rate, KL loss weight, and latent space dimension. The performance of model training is influenced jointly by the effectiveness of VAE in feature extraction and by the accuracy of MLP regression. Figure 1 and figure 2 show the result of the two-stage model training. After 50 and 100 training epochs, respectively, the training and validation losses of VAE and MLP steadily decreased and stabilized, showing no signs of overfitting (refer to figure 9). This indicates a reasonable capacity for feature extraction and regression. However, the reconstructed images from the test set exhibit noticeable discrepancies from the ground truth, suggesting that the current dataset may be not big enough for high-fidelity prediction.

While the model has not yet achieved high-accuracy predictions, the training process provides valuable insights into feature extraction and regression performance, laying the groundwork for future improvements.

DISCUSSION AND CONCLUSION

The nonlinear relationship between 3DPTF and its light redistribution is highly complex and difficult to simulate accurately using traditional software. This study proposes a data-driven approach that collect large-scale empirical data by automated optical experiments to train machine learning models. This research presents a systematic workflow for establishing a mapping between the physical parameters of 3DPTF (geometric attributes, incident light directions, observation coordinates, and fabrication parameters) and their resulting light distributions. The feasibility of this approach has been validated through parametric design, 3D printing, batch optical experiments, and machine learning. Although large-scale experiments have not been completed yet, this work offers insights for future research.

In the investigation of a single specimen, the automated robotic system for batch optical experiments demonstrated high efficiency. The VAE+MLP-based machine learning model proved effective in modeling light redistribution vs design variables. However, there is still room for improvement in model performance—potential enhancements include data augmentation, modifications to the loss function, and other optimization techniques. Additionally, as the study scales from a single specimen to multiple specimens, the increased data volume will require adjustments to the machine learning model architecture to accommodate greater complexity. A key challenge of mapping a low-dimensional input vector to a high-resolution luminance image, demands a capable data-driven model. In our experiments, the convergence of training results for a single sample indicates the model's effectiveness. However, to integrate all specimens into one coherent model, we recommend integrating physics-informed modules into the mapping process or exploring more advanced neural architectures, such as NeRF-based

variants (Mildenhall *et al*., 2020), to establish a more comprehensive mapping.

Building upon this study, future research will expand the dataset to include a greater variety of samples and incorporate additional 3D printing parameters. This will further validate the proposed methodology under larger and more complex parameter spaces while optimizing model training and optimization to ensure the robustness and scalability of the approach.

REFERENCES

Cheibas, I., D'Amico, B., Caldas, L., Seshadri, B. and Schlueter, A. (2023) 'Light Distribution in 3D-Printed Thermoplastics', *3D Printing and Additive Manufacturing*, 10(6), pp. 1164–1177. Available at: https://doi.org/10.1089/3dp.2023.0050.

Damirchi, H., Khorrambakht, R. and Taghirad, H.D. (2019) 'ARAS-IREF: An Open-Source Low-Cost Framework for Pose Estimation', in *2019 7th International Conference on Robotics and Mechatronics (ICRoM). 2019 7th International Conference on Robotics and Mechatronics (ICRoM)*, 16-18 September 2019, Tehran, Iran: IEEE, pp. 303–308. Available at: https://doi.org/10.1109/ICRoM48714.2019.9071852.

Huang, W., Wu, M., Lu, C., Dong, T. and Zhu, X. (2023) 'Review of Camera Calibration Methods and Their Progress', *Laser & Optoelectronics Progress*, 60(16), p. 1600001. Available at: https://doi.org/10.3788/LOP221494.

Jacobs, A. (2007) 'High Dynamic Range Imaging and its Application in Building Research', *Advances in Building Energy Research*, 1(1), pp. 177–202. Available at: https://doi.org/10.1080/17512549.2007.9687274.

Kurt, M. (2018) 'A Survey of BSDF Measurements and Representations', *Deu Muhendislik Fakultesi Fen ve Muhendislik*, 20(58), pp. 87–102. Available at: https://doi.org/10.21205/deufmd.2018205808.

Leschok, M., Hühne, T., Seshadri, B. and Schlueter, A. (2023) '3D printing facades: Design, fabrication, and assessment methods', *Automation in Construction*, 152, p. 104918. Available at: https://doi.org/10.1016/j.autcon.2023.104918.

Mildenhall, B., Srinivasan, P.P., Tancik, M., Barron, J.T., Ramamoorthi, R. and Ng, R. (2020) 'NeRF: Representing Scenes as Neural Radiance Fields for View Synthesis'. *arXiv*. Available at: https://doi.org/10.48550/ARXIV.2003.08934.

Mungenast, M.B. (2019) *3D-Printed Future Facade*. PhD thesis. Technische Universität München. Available at: https://mediatum.ub.tum.de/1456068.

Naboni, R. and Jakica, N. (2022) 'Additive manufacturing in skin systems: trends and future perspectives', in *Rethinking Building Skins*. Elsevier, pp. 425–451. Available at: https://doi.org/10.1016/B978-0-12-822477-9.00004-8.

Piccioni, V., Seshadri, B., Hühne, T., Leschok, M. and Schlueter, A. (2023) 'Challenges in modelling thermo-optical performance of 3D-printed facades: a cross-domain review'. Available at: https://doi.org/10.3929/ETHZ-B-000635325.

Piccioni, V., Seshadri, B., Leschok, M., Hühne, T. and Schlueter, A. (2023) 'Tuning the Solar Performance of Building Facades through Polymer 3D Printing: Toward Bespoke Thermo-Optical Properties', *Advanced Materials Technologies*, 8(6), p. 2201200. Available at: https://doi.org/10.1002/admt.202201200.

Pierson, C., Ibarra, D., Rogers, P. and Cotorica, B. (2021) 'Tutorial: Luminance Maps for Daylighting Studies from High Dynamic Range Photography', *LEUKOS*, 17(2), pp. 140–169. Available at: https://doi.org/10.1080/15502724.2019.1684319.

Seshadri, B., D'Amico, B., Cheibas, I., Leschok, M. and Schlueter, A. (2021) 'Parametric design of an

additively manufactured building facade for bespoke response to solar radiation', *Journal of Physics: Conference Series*, 2042(1), p. 012180. Available at: https://doi.org/10.1088/1742-6596/2042/1/012180.

Wang, T., Yang, H., Chen, X. and Cui, S. ((2022) 'Field validation of data-driven BSDF and peak extraction models for light-scattering fabric shades', *Energy and Buildings*, 262, p. 112002. Available at: https://doi.org/10.1016/j.enbuild.2022.112002.

Weber, R.E., Reinhart, C. and Oxman, N. (2020) 'Photon mapping of geometrically complex glass structures: Methods and experimental evaluation', *Building and Environment*, 180, p. 106957. Available at: https://doi.org/10.1016/j.buildenv.2020.106957.

Zhang, Z. (2000) 'A flexible new technique for camera calibration', *IEEE Transactions on Pattern Analysis and Machine Intelligence*, 22(11), pp. 1330–1334. Available at: https://doi.org/10.1109/34.888718.